Vibration Suppression and Trajectory Tracking with Nonlinear Model Predictive Control for UAM Aircraft

Jessica Nunes
Ph.D., ASME Student Member
Depart. of Aerospace Eng. and Mechanics
The University of Alabama
Tuscaloosa, Alabama 35487-0280
Email: jsnunes@crimson.ua.edu

Weihua Su
Associate Professor, Member of ASME
Depart. of Aerospace Eng. and Mechanics
The University of Alabama
Tuscaloosa, Alabama 35487-0280
Email: suw@eng.ua.edu

Tianyi He
Assistant Professor, Member of ASME
Depart. of Mechanical and Aerospace Eng.
Utah State University
Logan, Utah 84322
Email: tianyi.he@usu.edu

ABSTRACT

This paper describes developing and simulating a Nonlinear Model Predictive Controller (NMPC) for a tiltrotor urban air mobility (UAM) aircraft. The aircraft's free flight is governed by a set of nonlinear rigid-body dynamic equations, considering multiple tiltrotors and their gyroscopic and inertial effects. The control variables include two push rotors' spin rates and the deflections of traditional control surfaces, including the elevator, aileron, and rudder. The performance of the NMPC is compared with the Linear Quadratic Regulator (LQR) and Model Predictive Controller (MPC) for vibration suppression during the level flight. The NMPC and LQR can fully remove pitch angle oscillation and stabilize altitude in approximately 15 s*. The MPC, while still able to reduce the rigid body vibration cannot fully remove the oscillation in* 80 s*. The NMPC and LQR are compared for lateral and longitudinal trajectory path tracking, with the NMPC showing better performance in both cases*

due to its ability to take into account the nonlinear nature of the aircraft flight dynamics and predict the vehicle's future response when determining the best control inputs. Different from the vibration control case, the nonlinear nature of the aircraft flight dynamics should be accounted for by the controller design to properly track the ever-changing path reference, which is not the case for the LQR. While the NMPC has a higher computational cost, it demonstrates much better control performance than the MPC and LQR.

NOMENCLATURE

B Body coordinate frame

$\mathbf{p}_{G/B}$ Aircraft mass center position with respect to O_B, m

$\mathbf{v}_B$ Translational velocity vector, m/s

$\boldsymbol{\omega}_B$ Angular velocity vector, m/s

$\boldsymbol{\theta}_B$ Rigid-body rotation angles,rad

$\mathbf{M}_{BB}$ Inertia matrix

$\mathbf{C}_{BB}$ Damping matrix

$\mathbf{R}_B$ Aircraft load vector

$\mathbf{R}^{\text{grav}}$ Gravity load

$\mathbf{R}^{\text{iner}}$ Inertial loads

$\mathbf{R}^{\text{rate}}$ Induced moment due to tiltrotors

$\mathbf{R}^{\text{gyro}}$ Gyroscopic loads

$\mathbf{R}^{\text{ext}}$ External loads

$\boldsymbol{\Omega}_\zeta$ Rigid-body angular velocities function

$\mathbf{C}^{GB}$ Rotational matrix from the body to the global frame

$\epsilon_{\mathbf{0}}$ Nonlinear equilibrium solution

$\mathbf{u}_0$ Control input for equilibrium solution

$\mathbf{x}$ System states

$\mathbf{u}$ System control inputs

$\mathbf{y}$ System outputs

ϕ Roll angle, deg

θ Pitch angle, deg

ψ Yaw angle, deg

$\boldsymbol{\Phi}$ Euler angle vector

m_B Body mass, kg

I_B Body moment of inertia, kg m^2

m_r Rotor mass, kg

I_r^e Rotor moment of inertia, kg m^2

$\boldsymbol{\beta}$ Rigid-body velocity vector

$\boldsymbol{\zeta}$ Quaternions vector

$\mathbf{p}_B^G$ Inertial position vector of O_B, m

$\delta_e, \delta_a, \delta_r$ Elevator, aileron and rudder deflection, deg

$\boldsymbol{\Xi}$ Rotor tilt angle, deg

$\boldsymbol{\Gamma}$ Rotor spin angle, deg

A, B, C Continuous-time state space matrices

A_d, B_d, C_d Discrete-time state space matrices

dt Discretization time step

J Cost function

$\mathbf{Q}$ State weight matrix

$\mathbf{R}$ Input weight matrix

$\mathbf{K}$ LQR optimal gain matrix

$\mathbf{P}$ Riccati equation solution

$\mathbf{x}_D$ Desired state vector

$\mathbf{u}_D$ Desired input vector

$\mathbf{x}_0$ Nonlinear equilibrium condition states

$\mathbf{u}_0$ Nonlinear equilibrium condition inputs

$\tilde{\mathbf{x}}$ Error state vector

$\tilde{\mathbf{u}}$ Error input vector

$\mathbf{K}_{ss}$ LQR desired input matrix

p Prediction horizon

n Control horizon

$\mathbf{U}_k$ Quadratic problem decision vector

p Prediction horizon

n Control horizon

$\mathbf{r}$ Output reference vector

w^i Variable i NMPC weight

s^i Variable i NMPC scale factor

$u_{j,\text{target}}$ Target of the j^{th} input

$\mathbf{u}_{\text{min/max}}$ Input limits vector

$\Delta\mathbf{u}_{\text{min/max}}$ Input rate limits vector

INTRODUCTION

Recently, there has been a growing interest from industry and academia in urban air mobility (UAM) vehicles. This is due to their potential to be the solution for urban transportation in the near future. However, for UAM aircraft to truly become the future of aviation in urban areas, it is crucial to make significant advancements in flight safety, controllability, and flight automation. Several studies [1, 2, 3] highlight the need for these advancements to support the successful integration of UAM vehicles into urban airspace.

A specific category of these aircraft comprises distributed electric propulsion (DEP) enabled vertical takeoff/landing (VTOL) vehicles, commonly known as eVTOL vehicles [4]. These vehicles typically employ a fixed-wing design with multiple tiltrotors to allow them to perform such vertical takeoff and landing. In addition, the tilt and rotation capabilities of the rotors also serve as actuators for the aircraft. This unique characteristic offers several advantages for UAM eVTOL vehicles, including enhanced flight safety through control system redundancy, the potential for autonomous or semi-autonomous flights, and improved navigation in complex urban environments while avoiding obstacles [5]. However, these advancements introduce additional complexity to the design of the flight controller, underscoring the necessity for further research on novel and more robust control systems tailored for such applications.

Most published work on quadrotor [6, 7, 8, 9] and unmanned aerial vehicle (UAV) control [10, 11, 12, 13] used simple models, focusing on amplifying controller robustness and efficiency. For instance, the work by Baca et al. [14] utilized a linear model predictive controller to determine the optimal states needed to follow the desired path, instead of the control input, and used a nonlinear state-feedback controller to determine the input required to achieve such states. This approach achieved a short computational time of 2 to 10 ms per iteration. However, the vehicle model used in the study was relatively simple, with only attitude and thrust as states and the four rotors' thrust as input. While this methodology was successful for quadrotor unmanned aerial vehicles (UAVs), it did not have the complexity required for eVTOLs. Furthermore, quadrotors have the advantage of hovering in the air and flying backward if necessary. eVTOLs, while capable of hovering using the tiltrotors, require a transition period for the rotor tilting before it can perform

such actions, highlighting the need to consider the dynamics of the transition flight in the aircraft model.

Bertoncini et al. [15] focused on studying the use of NMPC in fixed-wing UAVs, but they did not take into account the tiltrotor aerodynamics. Additionally, their aircraft model only included the co-ordinate position and Euler angles as states, along with the aircraft's acceleration, rudder change rate, and pitch change rate as control inputs. However, the authors made an important contribution to developing control systems by integrating path-planning and cloud-detection algorithms.

Publications have recently been released on studying advanced controllers applied to more representative aircraft. The research conducted by He and Su [16] explored the use of MPC based on linear parameter-varying (LPV) models to suppress vibrations and alleviate gust loads for highly flexible aircraft experiencing wind gusts. They linearized the system dynamic equations and reduced them around various nonlinear equilibria to develop the reduced-order LPV models. The system models were then chosen based on a selection parameter. The main innovation of this work was the use of the magnitude of the first symmetric bending mode as the LPV scheduling parameter, compared to using the gust-induced angle of attack at the wing root. Both parameter selections were evaluated for gust alleviation when the flexible aircraft faced a uniformly applied gust perturbation across the entire wing. The control input was the conventional trailing-edge flaps on the main wings and tails. The simulation results demonstrated that the controller designed using the modal magnitude as LPV parameter performed better in suppressing gusts when compared to using the gust-induced angle of attack.

Qu et al. [17] also considered MPC based on LPV models, now applied for the hovering control of a six-rotor electric vertical takeoff and landing (eVTOL) urban air mobility aircraft subjected to motor failure. The aircraft model used in [17] is the same one presented in this paper. The models were obtained by linearizing the nonlinear rigid body model under different failed rotor speeds. The LPV scheduling parameter was a function of the failed rotor speed caused by available motor peak power after failure. This parameter could capture and describe the status of the system in the transition from healthy to failed propeller. The results showed that the designed adaptive MPC controller could recover and maintain the aircraft at the desired stable condition after motor failure

for all single motor failure cases. A better result was also observed when compared to the case of using only MPC, showing that the integration of LPV into the controller was beneficial. While this approach is effective for hovering control, it may be challenging for the linear controller to handle situations where the aircraft significantly deviates from the equilibrium condition, such as path tracking. This emphasizes the importance of the system's nonlinearities in the model used by the controller to predict future states.

The current study seeks to address the gap in the literature regarding the use of NMPC in eVTOL flight control for vibration suppression and path tracking. The aircraft used in this study is a complex hybrid eVTOL vehicle that features a fixed-wing aircraft configured with a six-tiltrotor DEP system. The aircraft's free flight motion is governed by a set of nonlinear rigid-body dynamic equations considering multiple tiltrotors and their gyroscopic and inertial effects, including the effect of tilting motion. Each rotor tilt angle and spin rate is available as an independent control input, in addition to the traditional aileron, elevator, and rudder inputs. The states consist of the three directional translation and rotational velocities, aircraft orientation quaternions, and the aircraft coordinates in space.

Moreover, the NMPC is a highly capable nonlinear controller that predicts future aircraft states and uses the prediction to determine the optimal input sequence to achieve the desired trajectory tracking and vibration control. The NMPC is compared to a Model Predictive Controller and a feedback Linear-Quadratic Regulator (LQR) in three simulation cases, including vibration suppression, lateral trajectory path tracking, and longitudinal trajectory path tracking.

This paper is organized as follows. Section 1 summarizes the nonlinear dynamic model for tiltrotor aircraft, including the system linearization, followed by the LQR, MPC, and NMPC formulations in Sect. 2. Section 3 presents LQR, MPC, and NMPC results for the simulation cases mentioned above. Finally, conclusions and future works are summarized in Sect. 4.

1 FLIGHT DYNAMIC FORMULATIONS

In this study, a hybrid UAM aircraft configured with a fixed wing and tiltrotors is considered (see Fig. 1). This paper briefly describes the flight dynamic equations of such a class of tiltrotor

vehicles, while a detailed derivation of the formulation can be found in Ref. [18].

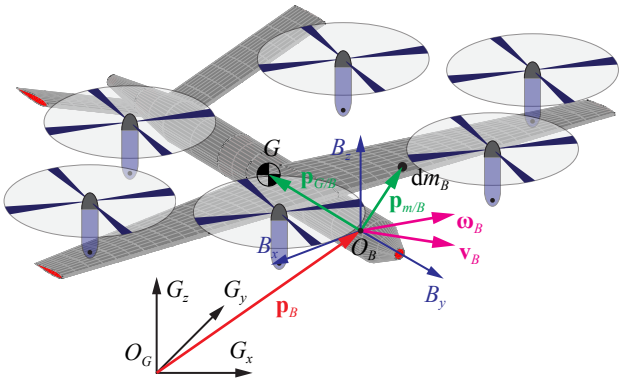

Fig. 1: Global and body reference frames of a rigid-body tiltrotor aircraft (connections between rotors and aircraft are not shown)

1.1 Nonlinear Flight Dynamic Formulation

First, a body-fixed frame B is defined with respect to the inertial frame G to describe the vehicle's position and orientation, with B_x pointing to the right wing, B_y pointing forward, and B_z completing the right-hand rule. While the B frame can be arbitrarily placed, it is convenient to set the frame's origin O_B within the vehicle's symmetric plane. The inertial position of O_B is represented by $\mathbf{p}_B$, while $\mathbf{p}_{G/B}$ describes the position of the mass center of the fixed-wing aircraft (excluding the tiltrotors) with respect to the B frame. The aircraft's rigid-body velocity is given by

$$\boldsymbol{\beta} = \begin{Bmatrix} \mathbf{v}_B \\ \boldsymbol{\omega}_B \end{Bmatrix} = \begin{Bmatrix} \dot{\mathbf{p}}_B + \boldsymbol{\omega}_B \times \mathbf{p}_B \\ \dot{\boldsymbol{\theta}}_B \end{Bmatrix} \tag{1}$$

By following the Hamilton's principle, the governing equation of motion is obtained, given by

$$\mathbf{M}_{BB}(\boldsymbol{\Xi})\dot{\boldsymbol{\beta}} + \mathbf{C}_{BB}(\boldsymbol{\beta}, \boldsymbol{\Xi})\boldsymbol{\beta} = \mathbf{R}_B \tag{2}$$

where the inertia matrix $\mathbf{M}_{BB}$ is dependent on the tilt angles $\boldsymbol{\Xi}$ of the rotors, while the damping matrix $\mathbf{C}_{BB}$ is dependent on both $\boldsymbol{\beta}$ and $\boldsymbol{\Xi}$. The load vector $\mathbf{R}_B$ is the summation of the loads about the B frame origin, including the contributions of gravity load $\mathbf{R}^{\text{grav}}$, inertial load $\mathbf{R}^{\text{iner}}$, induced moment due to tiltrotors $\mathbf{R}^{\text{rate}}$, gyroscopic load $\mathbf{R}^{\text{gyro}}$, and external load $\mathbf{R}^{\text{ext}}$, such as propulsive and aerodynamic loads, i.e.,

$$\mathbf{R}_B = \mathbf{R}^{\text{grav}} + \mathbf{R}^{\text{iner}} + \mathbf{R}^{\text{rate}} + \mathbf{R}^{\text{gyro}} + \mathbf{R}^{\text{ext}} \tag{3}$$

Details of these loads are found in Ref. [18]. In addition, the B frame's orientation is described by the quaternions $\boldsymbol{\zeta}$, governed by

$$\dot{\boldsymbol{\zeta}} = -\frac{1}{2}\boldsymbol{\Omega}_{\zeta}(\boldsymbol{\omega}_B)\boldsymbol{\zeta} \tag{4}$$

where $\boldsymbol{\Omega}_{\zeta}$ is a function of the rigid-body angular velocities $\boldsymbol{\omega}_B$, given by

$$\boldsymbol{\Omega}_{\boldsymbol{\zeta}}(\boldsymbol{\omega}_B) = \begin{bmatrix} 0 & \omega_B(1) & \omega_B(2) & \omega_B(3) \\ -\omega_B(1) & 0 & -\omega_B(3) & \omega_B(2) \\ -\omega_B(2) & \omega_B(3) & 0 & -\omega_B(1) \\ -\omega_B(3) & -\omega_B(2) & \omega_B(1) & 0 \end{bmatrix}. \tag{5}$$

Lastly, the inertial position of the B frame can be calculated by

$$\dot{\mathbf{p}}_B^G = \mathbf{C}^{GB}\mathbf{v}_B = \begin{bmatrix} \mathbf{C}^{GB} & \mathbf{0}_3 \end{bmatrix} \boldsymbol{\beta} \tag{6}$$

where $\mathbf{C}^{GB}$ is the rotational transformation matrix from the body to the global frame. The combination of Eqs. (2), (4), and (6) completes the nonlinear flight dynamic formulation of the tiltrotor

UAM aircraft. Those equations can be transformed to

$$\begin{aligned}
\dot{\boldsymbol{\beta}} &= \mathbf{M}_{BB}^{-1}\left(-\mathbf{C}_{BB}(\boldsymbol{\beta},\boldsymbol{\Xi})\boldsymbol{\beta} + \mathbf{R}_B(\boldsymbol{\beta},\dot{\boldsymbol{\beta}},\boldsymbol{\zeta},\delta_e,\delta_a,\delta_r,\boldsymbol{\Xi},\dot{\boldsymbol{\Xi}},\ddot{\boldsymbol{\Xi}},\dot{\boldsymbol{\Gamma}},\ddot{\boldsymbol{\Gamma}})\right) \\
\dot{\boldsymbol{\zeta}} &= -\frac{1}{2}\boldsymbol{\Omega}_{\zeta}(\boldsymbol{\beta})\boldsymbol{\zeta} \\
\dot{\mathbf{p}}_B^G &= \begin{bmatrix}\mathbf{C}^{GB} & \mathbf{0}_3\end{bmatrix}\boldsymbol{\beta}
\end{aligned} \tag{7}$$

where δ_e, δ_a and δ_r are the elevator, aileron, and rudder deflections, $\boldsymbol{\Xi}$ is the vector containing the rotor's tilt angles, and $\boldsymbol{\Gamma}$ is the vector of spin kinematics of the rotors. Therefore, the nonlinear system state and control input vectors are defined as follows,

$$\begin{aligned}
\boldsymbol{x}^T &= \left\{\boldsymbol{\beta}^T\ \dot{\boldsymbol{\beta}}^T\ \boldsymbol{\zeta}^T\ \dot{\boldsymbol{\zeta}}^T\ \left(\mathbf{p}_B^G\right)^T\ \left(\dot{\mathbf{p}}_B^G\right)^T\right\} \\
\mathbf{u}^T &= \left\{\delta_e\ \delta_a\ \delta_r\ \boldsymbol{\Xi}^T\ \dot{\boldsymbol{\Xi}}^T\ \ddot{\boldsymbol{\Xi}}^T\ \dot{\boldsymbol{\Gamma}}^T\ \ddot{\boldsymbol{\Gamma}}^T\right\}
\end{aligned} \tag{8}$$

As a post-processing, the Euler angles can be calculated from the quaternions. By keeping the convention of the Euler angles defined in the north-east-down (NED) frame for flight dynamics, the yaw angle ψ is defined as rotation about negative B_z-axis, the pitch angle θ is defined as rotation about B_x-axis, and the roll angle φ is defined as rotation about B_y-axis. Therefore, the Euler angles are given by

$$\begin{aligned}
\varphi &= \tan^{-1}\frac{2\left(\zeta_1\zeta_2 - \zeta_0\zeta_3\right)}{1-2\left(\zeta_0^2+\zeta_1^2\right)} \\
\theta &= \sin^{-1}\left[-2\left(\zeta_1\zeta_3 + \zeta_0\zeta_2\right)\right] \\
\psi &= \tan^{-1}\frac{2\left(\zeta_0\zeta_1 - \zeta_2\zeta_3\right)}{1-2\left(\zeta_1^2+\zeta_2^2\right)}
\end{aligned} \tag{9}$$

which can be simply noted as

$$\mathbf{\Phi} = \left\{ \varphi \ \theta \ \psi \right\}^T = \mathbf{\Phi}(\boldsymbol{\zeta}) \, . \tag{10}$$

Additionally, the system output $\boldsymbol{y}$ can be selected as a combination of system states and Euler angles, with the full form given by

$$\boldsymbol{y}^T = \left\{ \boldsymbol{\beta}^T \ \mathbf{\Phi}^T \ \left(\mathbf{p}_B^G \right)^T \right\} \tag{11}$$

1.2 Linearized Flight Dynamic Formulation

The trim solutions, either for level flight or vertical takeoff, were introduced in Ref. [18], which provide the steady-state solutions of the nonlinear equation set presented in the previous section. In general, one can take the Taylor's expansion on the nonlinear governing equations with respect to an equilibrium $\epsilon_{\mathbf{0}}$ with control input u_0, where $\epsilon_{\mathbf{0}}$ and $\mathbf{u}_0$ follow the presented in Eq. (8). After the Taylor's expansion, the equations of motion can be organized, leading to the linearized equations of motion [18], which is further written into the state-space form, given by

$$\begin{aligned} \Delta \dot{\mathbf{x}} &= \mathbf{A} \Delta \mathbf{x} + \mathbf{B} \Delta \mathbf{u} \\ \Delta \mathbf{y} &= \mathbf{C} \Delta \mathbf{x} \end{aligned} \tag{12}$$

The state, input, and output are small perturbations in relation to the nonlinear equilibrium. With the symbol Δ omitted, the system states and inputs are

$$\begin{aligned} \mathbf{x}^T &= \left\{ \boldsymbol{\beta}^T \ \boldsymbol{\zeta}^T \ \left(\mathbf{p}_B^G \right)^T \right\} \\ \mathbf{u}^T &= \left\{ \delta_e \ \delta_a \ \delta_r \ \mathbf{\Xi}^T \ \dot{\mathbf{\Xi}}^T \ \ddot{\mathbf{\Xi}}^T \ \dot{\mathbf{\Gamma}}^T \ \ddot{\mathbf{\Gamma}}^T \right\} \end{aligned} \tag{13}$$

The matrix $\mathbf{C}$ of Eq. (12) is selected according to the output vector to be tracked by the controller. If the full state vector is to be tracked, then $\mathbf{C} = \mathbf{I}_{13\times13}$.
Consider the forward Euler discretization equation

$$\dot{\mathbf{x}} \approx \frac{1}{dt}\left(\mathbf{x}_{k+1} - \mathbf{x}_k\right) \tag{14}$$

The state-space of Eq. (12) can then be discretized as follows

$$\begin{aligned} \mathbf{A_d} &= \mathbf{I} + \mathbf{A}dt \\ \mathbf{B_d} &= \mathbf{B}dt \end{aligned} \tag{15}$$

where dt is the discretization time step and $\mathbf{I}$ is an identity matrix with same dimension as $\mathbf{A}$. This results in the discrete system below with the Δ omitted

$$\begin{aligned} \mathbf{x}_{k+1} &= \mathbf{A}_d\mathbf{x}_k + \mathbf{B}_d\mathbf{u}_k \\ \mathbf{y}_{k+1} &= \mathbf{C}\mathbf{x}_k \ . \end{aligned} \tag{16}$$

2 CONTROL DEVELOPMENT

2.1 Linear-Quadratic Regulator

To derive state tracking dynamics, a set point control algorithm is formulated [19]. This formulation introduces the state and input error variables, given by

$$\begin{aligned} \tilde{\mathbf{x}}_k &= \mathbf{x}_k - \mathbf{x}_{D,k} \\ \tilde{\mathbf{u}}_k &= \mathbf{u}_k - \mathbf{u}_{D,k} \ . \end{aligned} \tag{17}$$

By substituting (17) into Eq. (16), a new state-space system is obtained with the error variables as state and input vectors and feedback control law $\tilde{\mathbf{u}}_k = -\mathbf{K}\tilde{\mathbf{x}}_k$, i.e.,

$$\tilde{\mathbf{x}}_{k+1} = \mathbf{A_d}\tilde{\mathbf{x}}_k + \mathbf{B_d}\tilde{\mathbf{u}}_k \ . \tag{18}$$

The infinite-horizon, discrete-time Linear-Quadratic Regulator (LQR) aims to minimize the quadratic cost function

$$J(\mathbf{u}) = \sum_{k=0}^{\infty} \left(\tilde{\mathbf{x}}_k^T \mathbf{Q_L} \tilde{\mathbf{x}}_k + \tilde{\mathbf{u}}_k^T \mathbf{R_L} \tilde{\mathbf{u}}_k\right) \tag{19}$$

where $\mathbf{Q_L}$ and $\mathbf{R_L}$ are the states and control input weight matrices for the LQR [20, 21]. The cross-term weight matrix is assumed to be zero and, therefore, omitted from the cost function. In this work, matrices $\mathbf{Q_L}$ and $\mathbf{R_L}$ are assumed to be diagonal matrices with $Q_{L,i}$ and $R_{L,i}$ as their diagonal terms.

Hence, the desired input $\mathbf{u}_{D,k}$ is obtained by solving [21]

$$\begin{aligned} \mathbf{u}_{D,k} &= \mathbf{K}_{ss}\mathbf{x}_{D,k} \\ \mathbf{K}_{ss} &= -\left(\mathbf{R} + \mathbf{B}_d^T \mathbf{P} \mathbf{B}_d\right)^{-1} \mathbf{B}_d^T \mathbf{P} \mathbf{A}_d \ . \end{aligned} \tag{20}$$

Substitute the new feedback control law and Eq. (17) into Eq. (18). The new closed-loop system is then obtained, i.e.,

$$\mathbf{x}_{k+1} = \left(\mathbf{A_d} - \mathbf{B_d}\mathbf{K}\right)\mathbf{x}_k - \left(\mathbf{A_d} - \mathbf{B_d}\mathbf{K}\right)\mathbf{x}_{D,k} \ . \tag{21}$$

This state-space system has the same states as Eq. (12). However, the control input is now the

desired state vector $\mathbf{x}_{D,k}$. The feedback control can also be rewritten to the form

$$\mathbf{u}_k = \mathbf{u}_{D,k} - \mathbf{K}\left(\mathbf{x}_k - \mathbf{x}_{D,k}\right) \tag{22}$$

As mentioned in Sect. 1.2, the linear aircraft model's states and inputs are small perturbations around the nonlinear equilibrium condition. Therefore, the LQR must follow the same convention, resulting in the final LQR formulation, given by

$$\begin{aligned} \mathbf{x}_{k+1} &= \left(\mathbf{A_d} - \mathbf{B_d}\mathbf{K}\right)\left(\mathbf{x}_k - \mathbf{x}_0\right) - \left(\mathbf{A_d} - \mathbf{B_d}\mathbf{K}\right)\left(\mathbf{x}_{D,k} - \mathbf{x}_0\right) \\ \mathbf{u}_{k+1} - \mathbf{u}_0 &= \left(\mathbf{u}_{D,k} - \mathbf{u}_0\right) - \mathbf{K}\left(\mathbf{x}_k - \mathbf{x}_{D,k}\right) \end{aligned} \tag{23}$$

where $\mathbf{x}_0$, and $\mathbf{u}_0$ are the states and inputs of the nonlinear equilibrium condition.

2.2 Nonlinear Model Predictive Controller

The nonlinear model predictive controller (NMPC) looks ahead by p steps to predict the dynamic system responses in the future (predicted output in Fig. 2). It then calculates the best sequence of control inputs $\mathbf{u}$ from the current time to time $t_n = t + n \times \mathrm{d}t$ to achieve the closest match between the system output and the desired output reference (predicted control input in Fig. 2) [22]. Here, p is the prediction horizon, and n is the control horizon. Figure 2 illustrates the NMPC control and prediction horizon. At each time step, the controller predicts the future system output and solves an optimization problem to determine the control input, using only the initial input vector (orange line). This procedure is then repeated in the next time step. This approach significantly enhances controller robustness, although it does come with the trade-off of increased computational cost.

In this study, the NMPC is designed using the MATLAB function *nlmpc* from the Model Predictive Control Toolbox [23]. The function *nlmpcmove* allows for solving the quadratic problem in each time step. The cost function of the quadratic problem behind the NMPC MATLAB toolbox

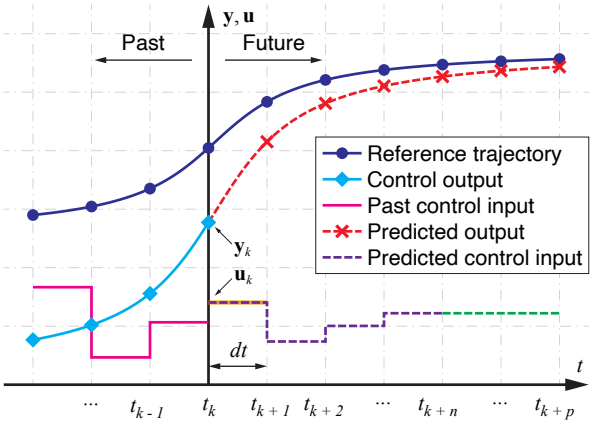

Fig. 2: NMPC control and prediction horizon

[24] has the form presented in

$$J(\mathbf{U}_k) = J_y(\mathbf{U}_k) + J_u(\mathbf{U}_k) + J_{\Delta u}(\mathbf{U}_k) \tag{24}$$

where $\mathbf{U}_k$ is the quadratic problem decision defined by

$$\mathbf{U}_k^T = \left\{ \mathbf{u}^T(k|k)\ \mathbf{u}^T(k+1|k)\ \ldots\ \mathbf{u}^T(k+p-1|k) \right\} \tag{25}$$

The $\mathbf{U}_k^T$ vector contains the inputs vectors $\mathbf{u}^T(k+i-1|k)$ calculated in the current control interval k for the i^{th} prediction horizon step, where i ranges from 1 to the prediction horizon p defined during the controller design.

The output reference tracking term J_y given by

$$J_y(\mathbf{U}_k) = \sum_{j=1}^{n_y} \sum_{i=1}^{p} \left\{ \frac{w_{i,j}^y}{s_j^y} \left[r_j(k+i|k) - y_j(k+i|k) \right] \right\}^2 \tag{26}$$

relates the j^{th} output reference $r_j(k+i|k)$ to the j^{th} output $y_j(k+i|k)$, both referent to the i^{th}

prediction horizon calculated at the current control interval k. The minimization of this term can be tuned by adjusting the weight for j^{th} plant output at the i^{th} prediction horizon step $w_{i,j}^{y}$ and the scale factor of the j^{th} output s_j^y. The cost function term J_u allows for tracking the input variable, given by

$$J_u(\mathbf{U}_k) = \sum_{j=1}^{n_u} \sum_{i=0}^{p-1} \left\{ \frac{w_{i,j}^{u}}{s_j^u} \left[u_j(k+i|k) - u_{j,\text{target}}(k+i|k) \right] \right\}^2 \tag{27}$$

where $u_{j,\text{target}}$ is the target value for the j^{th} input. $w_{i,j}^{u}$ and s_j^u are the weight and the scale factor of the j^{th} input. The third term of the cost function is given by

$$J_{\Delta u}(\mathbf{U_k}) = \sum_{j=1}^{n_u} \sum_{i=0}^{p-1} \left\{ \frac{w_{i,j}^{\Delta u}}{s_j^u} \left[u_j(k+i|k) - u_j(k+i-1|k) \right] \right\}^2 \tag{28}$$

which considers the input move suppression during the optimization process.

The NMPC is tuned for each case studied by adjusting the output and input weights. Those are considered constant throughout the prediction and control horizons and therefore have the new form w_j^y and w_j^u for the j^{th} output and j^{th} input weights. All the scale factors mentioned are kept at their default value of 1. The input movement weights $w_{i,j}^{\Delta u}$ are also kept at their default values of 0.1. While the NMPC formulation allows for output constraints, only input and input rate hard constraints are used in this work, i.e.,

$$\begin{aligned} u_{j,min}(i) \leq \ u_j(k+i-1|k) \ \leq u_{j,max}(i) \\ \Delta u_{j,min}(i) \leq \Delta u_j(k+i-1|k) \leq \Delta u_{j,max}(i) \end{aligned} \tag{29}$$

The scale factors were omitted from Eq. (31) since they were kept as units. In addition, uncertainties are neglected in the current work. In other words, the sensor data is assumed to be perfect reading without the noise usually present in practice. Note that, the stability and performance anal-

ysis of NMPC have been well studied in litetura [25, 26]. The effectiveness of the NMPC controller, combined with uncertainties, is recommended for future work.

2.3 Model Predictive Controller

Similar to NMPC, Model Predictive Control (MPC) also takes into account the predicted future system responses to determine the optimal system input (see Fig. 2). In this case, the prediction horizon p is equal to the control horizon n. However, unlike NMPC, MPC uses the linear system in its discrete-time form presented in Eq.(16). Therefore, the cost function to be minimized for the LQR-based MPC is given by

$$J(\mathbf{U}_k) = \mathbf{y}_n^T \mathbf{Q_f} \mathbf{y}_n + \sum_{k=0}^{n-1} \left(\mathbf{y}_k^T \mathbf{Q_M} \mathbf{y}_k + \mathbf{u}_k^T \mathbf{R_M} \mathbf{u}_k \right) \tag{30}$$

where $\mathbf{Q_f}$ is the terminal weighting matrix assumed to be an identity matrix, and $\mathbf{Q_M}$ and $\mathbf{R_M}$ are the states and control input weight matrices for the MPC [27]. The weight matrices are assumed to be diagonal matrices, similar to the LQR. $\mathbf{U}_k$ represents the control input sequence up to the control horizon, which is to be obtained from the problem minimization (see Eq. (25)).

In addition, the inputs are also subject to the hard constraints

$$\begin{aligned} \mathbf{u}_{min} \leq \ \mathbf{u}(t_k) \ &\leq \mathbf{u}_{max} \\ \Delta\mathbf{u}_{min} \leq \ \mathbf{u}(t_{k+1}) - \mathbf{u}(t_k) \ &\leq \Delta\mathbf{u}_{max} \end{aligned} \tag{31}$$

where $\mathbf{u}(k)$ is the control input vector at time t_k. An infeasible problem can occur when the controller cannot satisfy the optimization problem constraints. This means that it is mathematically impossible to meet the hard constraints while following the steady-state system equation of (16). Infeasibility may be due to an over-constrained system or a significant system disturbance, which can render the MPC unable to effectively control the dynamic system.

3 NUMERICAL STUDIES

This study focuses on the NMPC control of a UAM aircraft with six tiltrotors, as shown in Fig. 3. The aircraft's inertial and aerodynamic properties are listed in Tables 1 and 2, respectively. The rigid propeller pylon length is assumed to be $1\,$m. A comprehensive trim analysis at multiple flight conditions and the validation of the rotor tilt transition flight were investigated in a previous study (Ref. [18]) and will not be discussed here. The results showed that the aircraft model studied is stable and the formulation can capture the essential characteristics of rotor kinematics, such as tilt angle and spin rate, on the overall vehicle response.

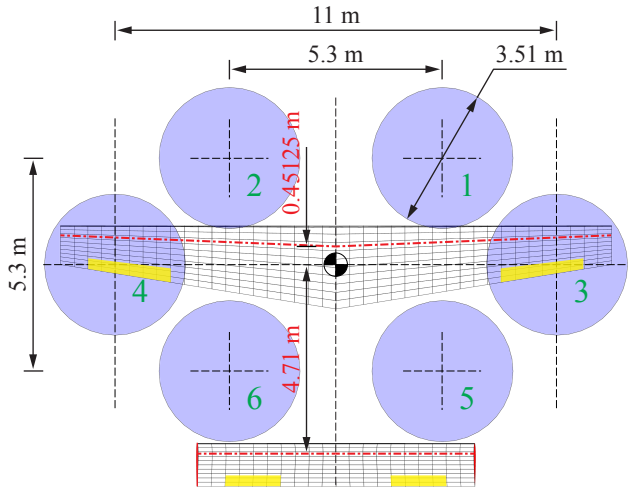

Fig. 3: Tiltrotor UAM aircraft geometry and rotor positions

The vehicle is first brought to a trimmed flight condition with a level flight speed of $68\,$m/s and an altitude of $304.8\,$m due North. This corresponds to a tip Mach number of 0.2 and a wing tip unit Reynolds number of $3.8 \times 10^6\ m^{-1}$. The chosen configuration has a lower flight speed and altitude than what is proposed in the literature for a similar class of airplane [28, 29]. In [28], an eVTOL UAM aircraft operated at flight speeds of $168\,$m/s and a cruise altitude of $3000\,$m above sea level, resulting in a tip Mach of 0.48 and a tip unit Reynolds number of $8.99 \times 10^6\ m^{-1}$. The reduced speed and altitude are selected in this work to consider the critical case of flying in a city setting closer to buildings and other obstacles. While obstacle avoidance is not considered herein, the flight condition is set to allow for its integration in the future. The NMPC will be evaluated in three

Table 1: Inertial properties of UAM aircraft.

Inertial Property	Value	Unit
Body mass, m_B	2,240.73	kg
Body moment of inertia, $I_{B,xx}$	12,000	kg m^2
Body moment of inertia, $I_{B,yy}$	9,400	kg m^2
Body moment of inertia, $I_{B,zz}$	20,000	kg m^2
Rotor mass, m_r	4.55	kg
Rotor moment of inertia, $I^e_{r,xx}$	3.5	kg m^2
Rotor moment of inertia, $I^e_{r,yy}$	7.0	kg m^2
Rotor moment of inertia, $I^e_{r,zz}$	3.5	kg m^2

Table 2: Aerodynamic properties of UAM aircraft.

Aerodynamic Property	Wing	Tail
Airfoil	NACA 0012	NACA 0012
Ref. axis location *	25%	25%
Span, m	13.72	6.90
Sweep angle, deg	-2.306	0
Dihedral angle, deg	0	0
Chord (root/tip), m	2.075/0.970	1.080/1.080
Incidence angle, deg **	3.1598	1.0626

* From leading-edge

** Incident angle with no twist

cases:

Vibration suppression (Sect. 3.1)

Lateral trajectory path tracking (Sect. 3.2)

Longitudinal trajectory path tracking (Sect. 3.3)

The NMPC is compared to the LQR for all three cases. The MPC is used to compare the vibration suppression analysis. During the level flight, rotors 3 and 4 remain in the forward position,

Table 3: Case ID and descriptions for vibration suppression and path tracking

Case ID	Description
O-VIB	Open loop - vibration suppression
L-VIB	LQR - vibration suppression
M-VIB	MPC - vibration suppression
N-VIB	NMPC - vibration suppression
O-VIB-30	Open loop - vibration suppression with 30% of elevator excitation
M-VIB-30	MPC - vibration suppression with 30% of elevator excitation
L-LAT	LQR - lateral trajectory path tracking
N-LAT	NMPC - lateral trajectory path tracking
L-LON	LQR - longitudinal trajectory path tracking
N-LON	NMPC - longitudinal trajectory path tracking

working as push rotors, with their spin rates as control inputs to generate the required thrust. The other rotors are turned off and are not used as input by the controllers. Therefore, the control input vector is reduced to

$$\mathbf{u}^T = \left\{ \delta_e \ \delta_a \ \delta_r \ \dot{\Gamma}_3 \ \dot{\Gamma}_4 \right\} \tag{32}$$

for both the nonlinear and linear models, where $\dot{\Gamma}_3$ and $\dot{\Gamma}_4$ are the spin rates of rotors 3 and 4, respectively. The system states are kept the same as Eq. (13).

A case ID will be used to identify the simulations cases, following the naming convention "1-2-3" where "1" means open-loop (O), LQR (L), MPC (M), or NMPC (N) results. "2" informs on the nature of the simulation with VIB for vibration suppression, LAT for lateral path tracking and LON for longitudinal path tracking, and "3" provides addition information, when applicable. A description of the simulation cases and IDs is presented in Table 3 and the open loop and controllers settings are summarised in Appendix 4.

3.1 Vibration Suppression

The NMPC output vector $\mathbf{y}$ is

$$\mathbf{y}^T = \left\{ \phi \; \theta \; \psi \; p_{B,x}^G \; p_{B,z}^G \right\} \tag{33}$$

where ϕ, θ, and ψ are the roll, pitch, and yaw angles in degrees, and $p_{B,x}^G$ and $p_{B,z}^G$ are the B frame inertial position in the lateral and vertical directions, respectively, measured in meters. For the LQR and MPC, the system output is given by

$$\mathbf{y}^T = \left\{ \boldsymbol{\beta}^T \; \phi \; \theta \; \psi \; p_{B,x}^G \; p_{B,z}^G \right\} \tag{34}$$

The phugoid mode of the aircraft is excited by an elevator input in degrees, given by

$$\delta_e = \begin{cases} \delta_{e,0} & t < 0.01\,\text{s} \\ \delta_{e,0} + 2\left[1 - \cos\left(\dfrac{2}{5}\pi\,(t - 0.01)\right)\right] & 0.01\,\text{s} \leq t \leq 5.01\,\text{s} \\ \delta_{e,0} & t > 5.01\,\text{s} \end{cases} \tag{35}$$

The resulting open-loop longitudinal behavior of the aircraft can be observed in Fig. 4 (see the green dashed lines). In the closed-loop simulations, the controllers (LQR, MPC, or NMPC) are engaged since $t = 5.01\,\text{s}$, which is marked by a vertical dotted line in the figures. All inputs and system responses before $t = 5.01\,\text{s}$ are identical for all cases, with and without controllers. The controllers are tasked with suppressing the phugoid mode vibration by returning the output $\mathbf{y}$ to its initial trimmed flight condition $\mathbf{y}_0$.

The weight matrices $\mathbf{Q}$ and $\mathbf{R}$ for the LQR and MPC are provided in Table 4. Both are simulated using a time step of $0.01\,\text{s}$. Meanwhile, the NMPC uses a time step of $0.1\,\text{s}$. As for the optimization problem solver, both the MPC and NMPC utilize *fmincon*, a solver in MATLAB's Op-

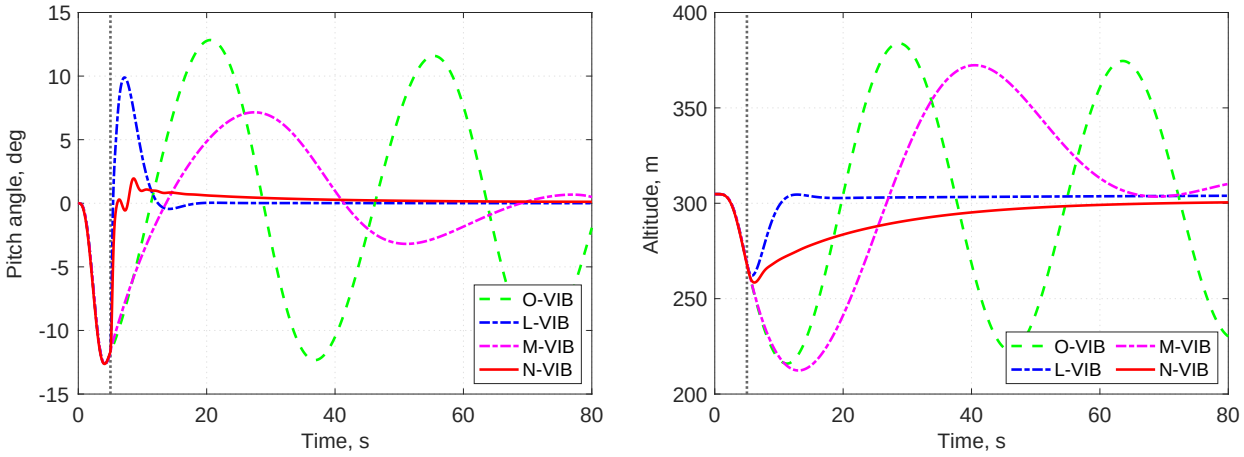

Fig. 4: Pitch angle and altitude responses during vibration suppression simulation

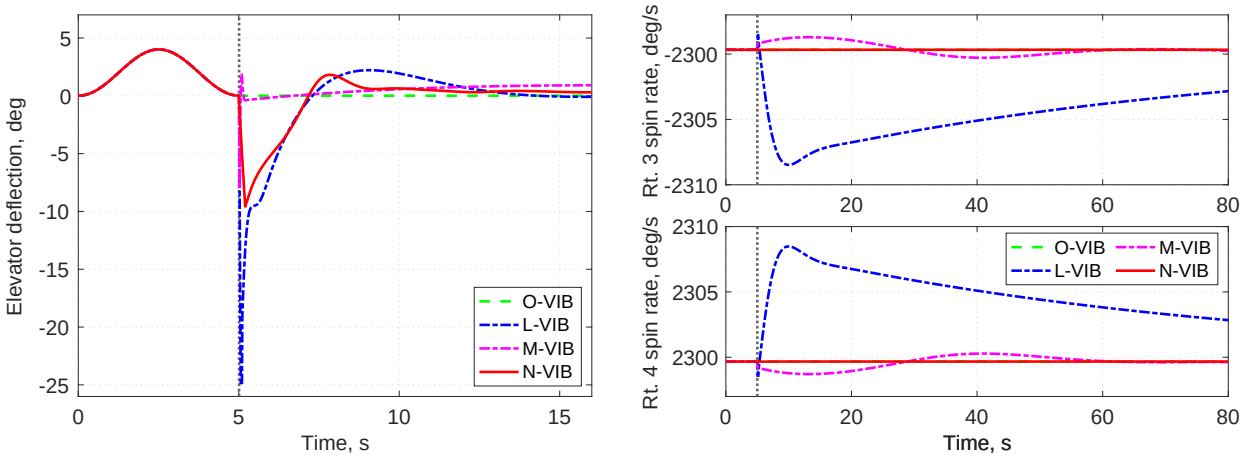

Fig. 5: Elevator deflection and spin rate inputs for vibration suppression

timization Toolbox used to find the minimum of a constrained scalar function of multiple variables. The input and output weights for the NMPC can be found in the Appendix.

Figures 5 show the open loop, LQR, MPC, and NMPC inputs for the vibration suppression case. Since the vibration is longitudinal, the aileron and rudder control surfaces are not actuated. For the same reason, only the pitch angle and altitude are presented (refer to Fig. 4). The elevator deflection is presented in Fig. 5 only up to $16\,$s to allow for observation of the δ_e input in detail. After $16\,$s of simulation, both LQR and NMPC elevator inputs remain constant, while MPC elevator input shows low-frequency oscillation. Figure 4 shows that the NMPC can nearly instantly return

Table 4: Parameter of LQR and MPC for the vibration suppression simulation case.

Controller	Property	Value
LQR	Q_1 to Q_7, Q_9 to Q_{10}	1
	Q_8 and Q_{11}	0.01
	R_1	500
	R_2 to R_5	1
MPC	Q_1 to Q_7, Q_9 to Q_{11}	1
	Q_8	150
	R_1 to R_5	1

the pitch angle to its initial condition with minimal overshooting. The altitude gradually returns to a constant value, stabilizing at $300\,$m of altitude at approximately $60\,$s of simulation. While a stable altitude is obtained, it is $2\,$m below target value. The LQR, on the other hand, returns both outputs to their desired initial condition in approximately $15\,$s after the controller is activated. The LQR takes advantage of the spin rates inputs, while the NMPC keeps these inputs constant.

Although the MPC was able to reduce the phugoid mode vibration compared to the open-loop response, it was unable to fully remove the rigid body oscillation during the $80\,$s simulation. Varying the $\mathbf{Q}_\mathrm{M}$ and $\mathbf{R}_\mathrm{M}$ MPC weight matrices diagonal values, changing the simulation time-step, or adjusting the MPC prediction horizon caused the MPC to be infeasible in most combinations, showing that the window at which the MPC is feasible for this system with this level of system disturbance is relatively small. The MPC was tested with a reduced excitation scenario, where the elevator input is set to 30% of the elevator input in Eq. (34). The controller settings in Table 4 were used for this test. Figures 6 and 7 show the comparison between the system response and inputs for both the open-loop and MPC cases. When the system excitation is lower, the MPC is able to bring the system response closer to a constant value. However, even with only 30% of the excitation, the oscillation was not eliminated during the simulation.

In summary, both LQR and NMPC are viable for vibration suppression. On the other hand, the MPC formulation used was proven unsuitable for this application when the system is subjected to higher excitation. Therefore, the MPC will be omitted from the path tracking cases, which are

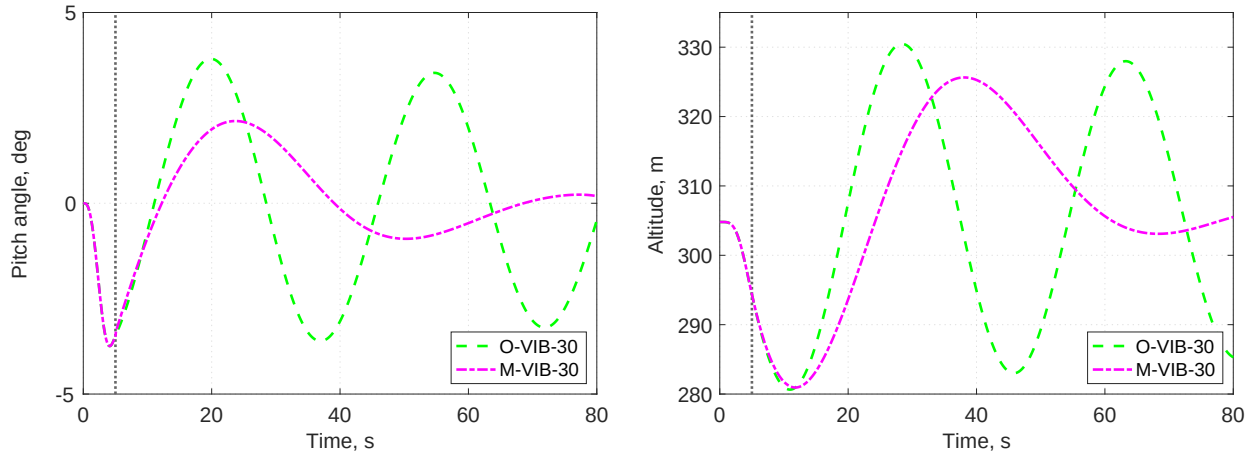

Fig. 6: Pitch angle and altitude responses during vibration suppression simulation with 30% of elevator excitation

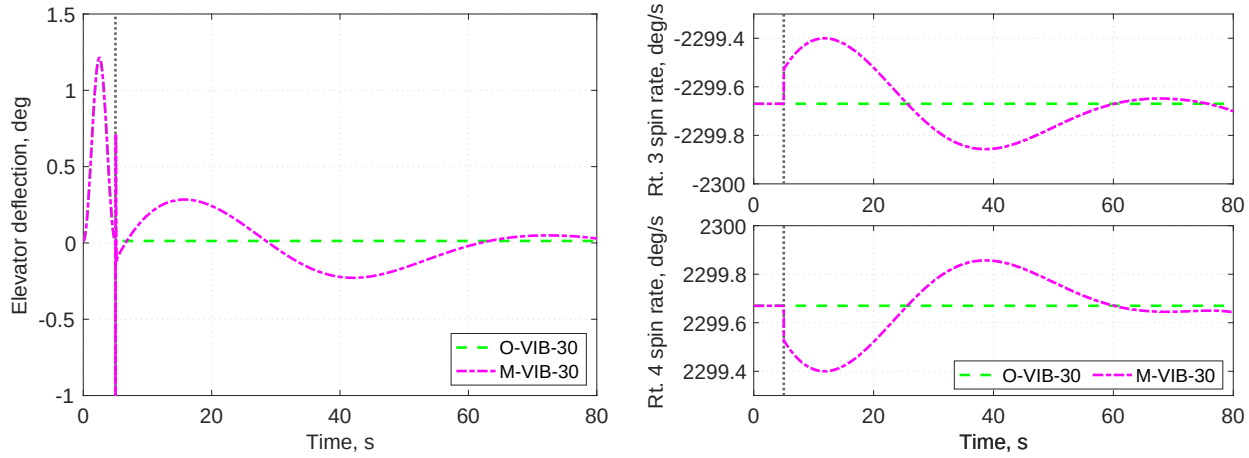

Fig. 7: Elevator deflection and spin rate inputs for vibration suppression with 30% of elevator excitation

expected to be more challenging scenarios.

3.2 Lateral Trajectory Path Tracking

For lateral path tracking, the north-wise aircraft position $p^G_{B,y}$ (in meters) is added to the system outputs, resulting in

$$\mathbf{y}^T = \left\{ \phi \; \theta \; \psi \; p^G_{B,x} \; p^G_{B,y} \; p^G_{B,z} \right\} \tag{36}$$

Table 5: LQR setting for the lateral trajectory simulation case.

Property	Value
Q_1 to Q_6	0
Q_7,Q_8, Q_{10} to Q_{12}	1
Q_9	100
R_1	100
R_2 to R_5	50

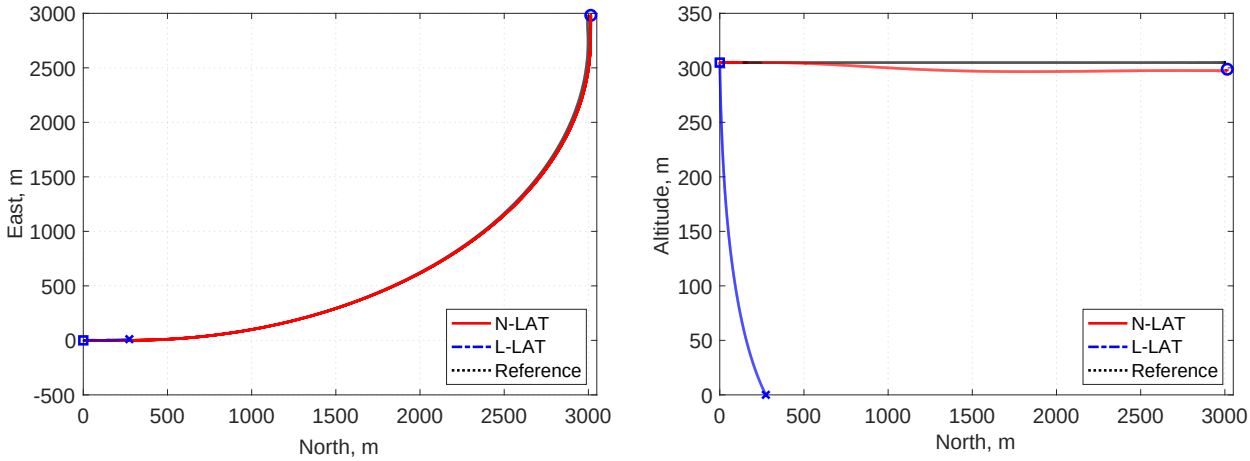

Fig. 8: Aircraft lateral trajectory for LQR and NMPC

for the NMPC, and the vector of Eq. (34) with $p^G_{B,y}$ for the LQR. This case is simulated for $70\,\mathrm{s}$, and the NMPC input target is the initial input condition. The lateral curve consists of a level flight with flight speed due north for $2\,\mathrm{s}$, followed by a curve to the right in the horizontal plane until a yaw angle of $90°$ is achieved. Then, a second level flight with speed due east is tracked for the remaining simulation of $4\,\mathrm{s}$. The reference output $\mathbf{y}_{\mathrm{ref}}$ is defined by Eqs. (37) to (40). The time intervals for each stage of the curve are arbitrarily selected while ensuring a gradual curve to the right with time enough for the controller to achieve stable flight conditions. The output x and y coordinate reference curves are defined by running the open-loop simulation of the aircraft when following the desired Euler angle outputs. The reference pitch angle θ_{ref} and altitude $\left(p^G_{B,z}\right)_{\mathrm{ref}}$ are kept the same as the trimmed flight condition.

The $\mathbf{Q}$ and $\mathbf{R}$ matrices for the LQR controller are shown in Table 5, and the NMPC input and

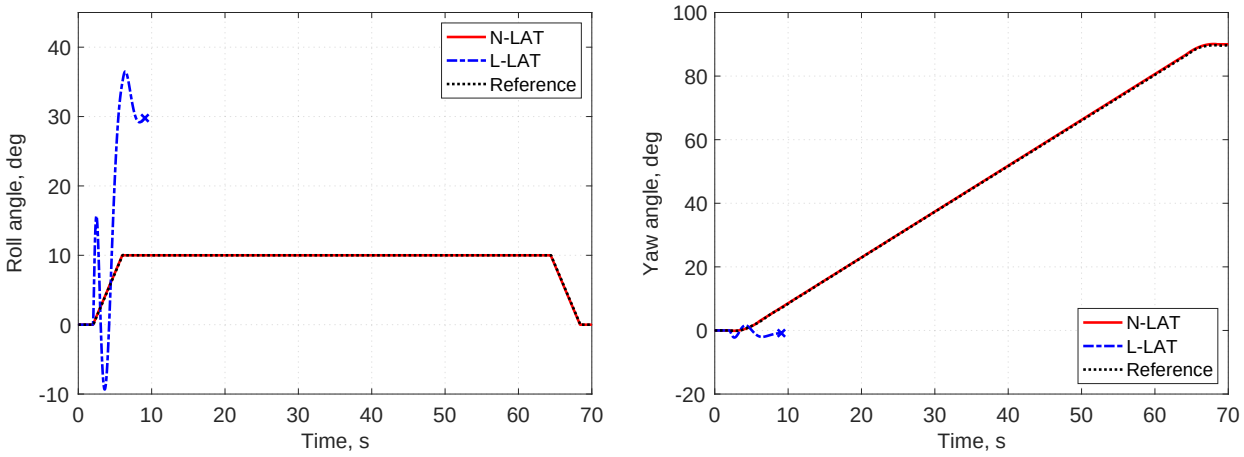

Fig. 9: Roll and yaw angle responses to lateral trajectory tracking

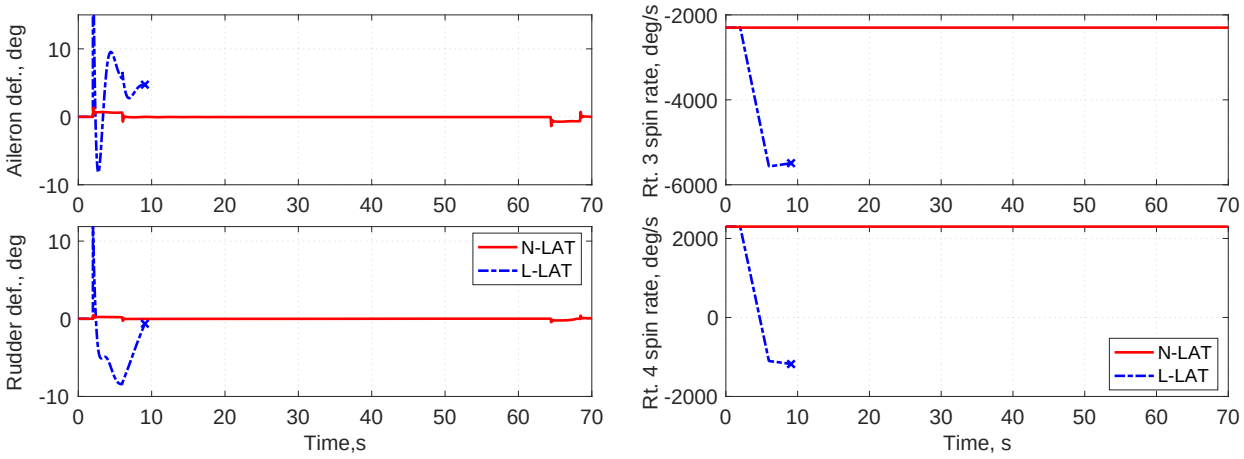

Fig. 10: Aileron, rudder deflection and spin rate inputs for lateral trajectory tracking

output weights are presented in the Appendix. Both controllers are simulated using a time step of 0.01 s. Figures 8 and 9 present the flight trajectory and Euler angles responses. The X (cross) in the LQR curve highlights the point at which the aircraft contacts the ground (see the altitude of zero in Fig. 8). The aileron deflection, rudder deflection, and rotor spin rates (Fig. 10) are the control inputs involved in this lateral flight.

The NMPC presents a smaller control cost with maximum aileron and rudder deflection magnitudes of $1.37°$ and $0.47°$, respectively. The tiltrotor spin rates are approximately constant for the NMPC. On the other hand, the LQR reaches a maximum aileron and rudder deflection magnitude

of $28.76°$ and $100.58°$, respectively. A high magnitude is also observed for the tiltrotor spin rates. Even with such a high control cost, the LQR is unable to track the output references of the roll and yaw angles (Fig. 9). That is expected since the LQR uses the linear UAM aircraft system. As the system deviates further from the steady state, the linear model accuracy in approximating the non-linear aircraft dynamic declines. The results show that the NMPC can accurately track the lateral path with minor deviation in altitude, which is quickly recovered back to the desired value, while the LQR is unable to do so, showing a large drop in altitude resulting in the crash at approximately $10\,$s of simulation (Fig. 9).

$$\phi_{ref} = \begin{cases} \phi_0\,° & t < 2\,\text{s} \\ 2.5t - 5\,° & 2\,\text{s} \leq t < 6\,\text{s} \\ 10\,° & 6\,\text{s} \leq t < 62\,\text{s} \\ -2.5t - 165\,° & 62\,\text{s} \leq t < 66\,\text{s} \\ \phi_0\,° & t \geq 66\,\text{s} \end{cases} \tag{37}$$

$$\psi_{ref} = \begin{cases} \psi_0\,° & t < 2\,\text{s} \\ 0.24t^2 - 1.22t + 1.45\,° & 2\,\text{s} \leq t < 6\,\text{s} \\ 1.44t - 5.87\,° & 6\,\text{s} \leq t < 62\,\text{s} \\ -0.23t^2 + 31.53t - 982.54\,° & 62\,\text{s} \leq t < 66\,\text{s} \\ 90\,° & t \geq 66\,\text{s} \end{cases} \tag{38}$$

$$\left(p_{B,x}^{G}\right)_{ref} = \begin{cases} \left(p_{B,x}^{G}\right)_0 \,\mathsf{m} & t < 2\,\mathsf{s} \\ -3.55 \times 10^{-5} t^4 + 6.98 \times 10^{-5} t^3 + 0.88 t^2 - 7.13 t + 14.71 \mathsf{m} & 2\,\mathsf{s} \leq t < 66\,\mathsf{s} \\ 69t - 1.84 \times 10^3 \mathsf{m} & t \geq 66\,\mathsf{s} \end{cases} \tag{39}$$

$$\left(p_{B,y}^{G}\right)_{ref} = \begin{cases} 68t\,\mathsf{m} & t < 2\,\mathsf{s} \\ 3.3 \times 10^{-5} t^4 - 9.67 \times 10^{-3} t^3 + 0.17 t^2 + 66.77 t + 3.06 \mathsf{m} & 2\,\mathsf{s} \leq t < 66\,\mathsf{s} \\ 2995\,\mathsf{m} & t \geq 66\,\mathsf{s} \end{cases} \tag{40}$$

3.3 Longitudinal Trajectory Tracking

The simulation for longitudinal trajectory tracking takes the same output vector of Eq. (33), with a simulation duration of $180\,\mathsf{s}$. The trajectory to be tracked consists of a level flight with a speed of $68\,\mathsf{m/s}$ due north at the altitude of $304.8\,\mathsf{m}$ up to $5\,\mathsf{s}$ of simulation. That is followed by a $2.54\,\mathsf{m/s}$ linear climb path up to $150\,\mathsf{s}$ of simulation. Thereafter, a different level flight starts at an altitude of $673.1\,\mathsf{m}$. This climb rate is in accordance with the literature for eVTOL aircraft [30]. The reference curves for the pitch angle and vertical inertial position are given by

$$\theta_{ref} = \begin{cases} \theta_0\,^\circ & t < 5\,\mathsf{s} \\ \theta_{climb}\,^\circ & 5\,\mathsf{s} \leq t < 150\,\mathsf{s} \\ \theta_0\,^\circ & t \geq 150\,\mathsf{s} \end{cases} \tag{41}$$

Table 6: LQR setting for the longitudinal trajectory simulation case.

Property	Value
Q_1 to Q_7, Q_8 to Q_{11}	1
Q_8	100
Q_{12}	50
R_1	10^4
R_2 to R_5	10

$$\left(p^G_{B,z}\right)_{ref} = \begin{cases} \left(p^G_{B,z}\right)_0 \text{ m} & t < 5\,\text{s} \\ \left(p^G_{B,z}\right)_0 + 2.54 \times (t-5)\text{m} & 5\,\text{s} \leq t < 150\,\text{s} \\ 673.1\text{m} & t \geq 150\,\text{s} \end{cases} \tag{42}$$

The roll angle, yaw angle, and east-wise positions $\left(p^G_{B,x}\right)_{\text{ref}}$ references are kept constant at 0 since this is a purely longitudinal flight path. The NMPC input target is the initial input condition $\boldsymbol{u_0}$ during level flight and the trimmed climb condition $\boldsymbol{u_{climb}}$ during the climb. The $\mathbf{Q}$ and $\mathbf{R}$ matrices for the LQR controller are provided in Table 6, while the NMPC input and output weights can be found in the Appendix. Both controllers are simulated using a time step of $0.01\,$s.

The control inputs of main importance in the longitudinal path case are the elevator deflection and tiltrotors spin rate (Fig. 11). Similarly to the previous 2 cases, the LQR showed higher control cost, reaching spin rate magnitudes of up to 8000 °/s. Even with such high control inputs, the LQR cannot track the reference pitch angle, showing some deviation from the desired flight path (Fig. 12). An initial vertical position drop in the first $8\,$s of flight leads to a deviation of altitude and north-wise position, which is not recovered by the end of the simulation. On the other hand, the NMPC shows excellent path tracking (Fig. 12) while requiring lower control input magnitudes (Fig. 11). The NMPC shows small overshooting following the transition from level flight to climb. A maximum pitch angle deviation from the reference of $\pm\ 0.7°$ is observed. Consequently, the

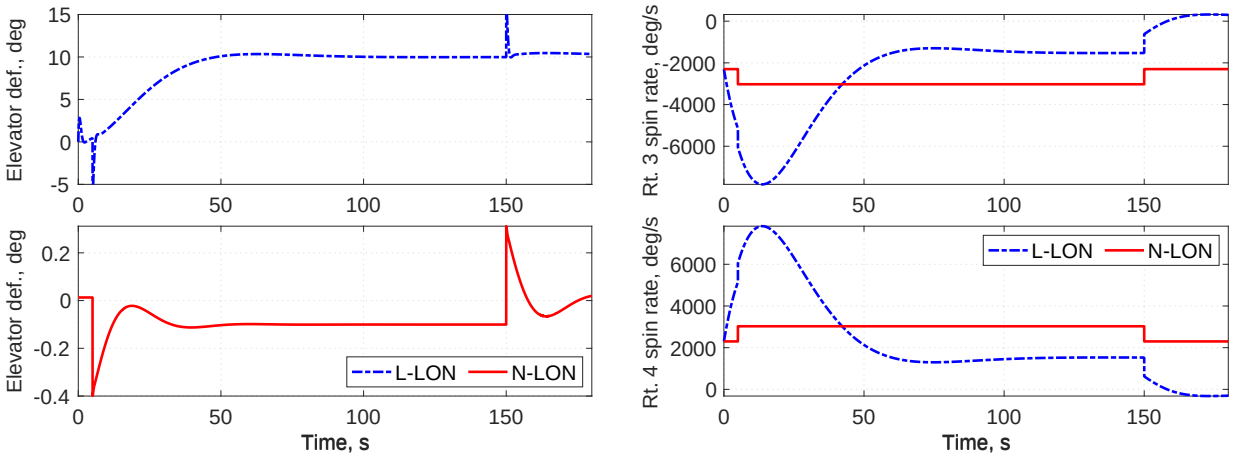

Fig. 11: Elevator deflection and rotor spin rate to longitudinal trajectory tracking

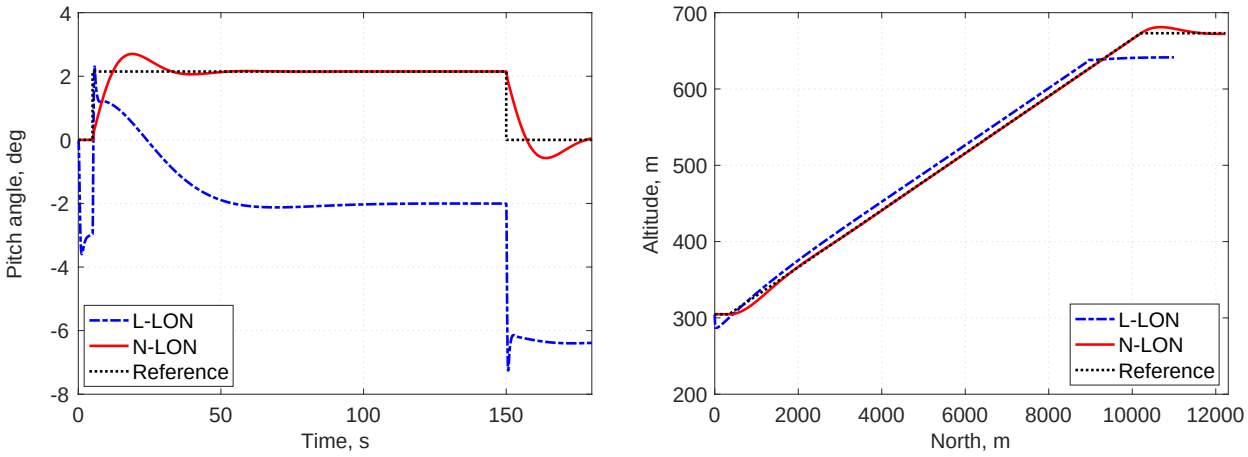

Fig. 12: Pitch angle and aircraft longitudinal trajectory for LQR and NMPC

vertical position has a deviation of up to $\pm$ 8 m following the flight transition.

4 CONCLUSIONS

This paper presented the implementation of a Nonlinear Model Predictive Controller (NMPC) for an urban air mobility (UAM) aircraft. The NMPC was tested for suppression of the excited phugoid vibration mode, lateral trajectory tracking, and longitudinal trajectory tracking. The results were compared with a Linear-Quadratic Regular (LQR) modified to allow for state tracking and reduce control overshooting, and with an LQR-based Model Predictive Controller (MPC). The

results showed that the NMPC and LQR had similar control effectiveness in the vibration suppression case, while the MPC was ineffective in removing the rigid body oscillation after $80\,\mathrm{s}$ of simulation. Even for the case with system excitation 70% lower, the MPC was still unable to fully remove the system oscillation, proving the proposed formulation to be unfeasible for this application. When comparing the NMPC and LQR for path tracking, the NMPC was more effective than the LQR because the latter uses the linearized version of the nonlinear tiltrotor aircraft dynamic model, which becomes increasingly inaccurate as the system gets further away from the initial steady-state condition.

In conclusion, this study has shown that NMPC is suitable for suppressing vibrations and tracking the path of eVTOL aircraft. However, the high computational cost of NMPC remains a challenge, preventing real-time use of this controller during flight. Currently, it takes $8\,\mathrm{h}$ to compute a $60\,\mathrm{s}$ flight simulation, highlighting the need for further research on computational optimization. Neural Network-based NMPC has the potential to significantly reduce computational time, and such an approach is currently under investigation for future work. Additionally, the assessment of NMPC for controlling eVTOL in the event of control input failure during flight, and for flight control under gust excitation, are also under investigation for future work.

REFERENCES

[1] Holden, J., and Goel, N., 2016, Fast-forwarding to a future of on-demand urban air transportation. Tech. rep., UBER Company, Elevate project.

[2] Zhou, Y., Zhao, H., and Liu, Y., 2020, "An evaluative review of the VTOL technologies for unmanned and manned aerial vehicles," *Computer Communications,* **149**, pp. 356–369.

[3] Straubinger, A., Rothfeld, R., Shamiyeh, M., Büchter, K.-D., Kaiser, J., and Plötner, K. O., 2020, "An overview of current research and developments in urban air mobility – setting the scene for uam introduction," *Journal of Air Transport Management,* **87**, p. 101852.

[4] Kim, H. D., Perry, A. T., and Ansell, P. J., 2018, "A review of distributed electric propulsion concepts for air vehicle technology," In 2018 AIAA/IEEE Electric Aircraft Technologies Symposium (EATS), IEEE, pp. 1–21.

[5] Zhao, Y., Guo, J., Bai, C., and Zheng, H., 2021, "Reinforcement learning-based collision avoidance guidance algorithm for fixed-wing uavs," *Complexity journal,* **2021**(8818013), pp. 1–12.

[6] Yu, X., Zhu, W., and Xu, L., 2020, "Real-time motion planning and trajectory tracking in complex environments based on Bézier curves and nonlinear MPC controller," In 2020 Chinese Control And Decision Conference (CCDC), IEEE, pp. 1540–1546.

[7] Carlos, B. B., Sartor, T., Zanelli, A., Frison, G., Burgard, W., Diehl, M., and Oriolo, G., 2020, "An efficient real-time NMPC for quadrotor position control under communication time-delay," In 2020 16th International Conference on Control, Automation, Robotics and Vision (ICARCV), IEEE, pp. 982–989.

[8] Nascimento, I. B. P., Ferramosca, A., Pimenta, L. C. A., and Raffo, G. V., 2019, "NMPC strategy for a quadrotor uav in a 3d unknown environment," In 2019 19th International Conference on Advanced Robotics (ICAR), IEEE, pp. 179–184.

[9] Zhang, K., Shi, Y., and Sheng, H., 2021, "Robust nonlinear model predictive control based visual servoing of quadrotor UAVs," *IEEE/ASME Transactions on Mechatronics,* **26**(2), pp. 700–708.

[10] Soni, D., Manoharan, A., Tyagi, P., and Sujit, P., 2022, "Learning-based NMPC framework for car racing cinematography using fixed-wing UAV," In 2022 International Conference on Unmanned Aircraft Systems (ICUAS), IEEE, pp. 1397–1403.

[11] Gros, S., Quirynen, R., and Diehl, M., 2012, "Aircraft control based on fast non-linear MPC & multiple-shooting," In 2012 IEEE 51st IEEE Conference on Decision and Control (CDC), IEEE, pp. 1142–1147.

[12] Garcia, G., Keshmiri, S., and Stastny, T., 2015, "Nonlinear model predictive controller robustness extension for unmanned aircraft," *International Journal of Intelligent Unmanned Systems,* **3**(2/3), pp. 93–121.

[13] Basescu, M., and Moore, J., 2020, "Direct nmpc for post-stall motion planning with fixed-wing UAVs," In 2020 IEEE International Conference on Robotics and Automation (ICRA), IEEE, pp. 9592–9598.

[14] Baca, T., Hert, D., Loianno, G., Saska, M., and Kumar, V., 2018, "Model predictive trajectory tracking and collision avoidance for reliable outdoor deployment of unmanned aerial vehicles," In 2018 IEEE/RSJ International Conference on Intelligent Robots and Systems (IROS), IEEE, pp. 6753–6760.

[15] Bertoncini, J., Dudek, A., Russ, M., Gerdts, M., and Stütz, P., 2023, "Fixed-wing UAV path planning and collision avoidance using nonlinear model predictive control and sensor-based cloud detection," In 2023 IEEE/AIAA 42nd Digital Avionics Systems Conference (DASC), IEEE, pp. 1–10.

[16] He, T., and Su, W., 2023, "Robust control of gust-induced vibration of highly flexible aircraft," *Aerospace Science and Technology,* **143**, p. 108703.

[17] Qu, S., Zhu, G., Su, W., Shan-Min Swei, S., Hashimoto, M., and Zeng, T., 2022, "Adaptive model predictive control of a six-rotor electric vertical take-off and landing urban air mobility aircraft subject to motor failure during hovering," *Proceedings of the Institution of Mechanical Engineers, Part G: Journal of Aerospace Engineering,* **236**(7), pp. 1396–1407.

[18] Su, W., Qu, S., Zhu, G., Swei, S. S.-M., Hashimoto, M., and Zeng, T., 2022, "Modeling and control of a class of urban air mobility tiltrotor aircraft," *Aerospace Science and Technology,* **124**, p. 107561.

[19] Haber, A., 2021, Compute and simulate linear quadratic regulator (LQR) in MATLAB for nonzero set points.

[20] Kwakernaak, H., Sivan, R., and Tyreus, B. N. D., 1974, "Linear optimal control systems,".

[21] Lewis, F. L., Vrabie, D., and Syrmos, V. L., 2012, *Optimal control* John Wiley & Sons.

[22] Takács, G., and Rohal'-Ilkiv, B., 2012, *Model predictive vibration control: efficient constrained MPC vibration control for lightly damped mechanical structures* Springer Science & Business Media.

[23] MathWorks, Accessed 2022-09-05, Model predictive control toolbox.

[24] MathWorks, Accessed 2022-11-23, Optimization problem.

[25] Köhler, J., Zeilinger, M. N., and Grüne, L., 2023, "Stability and performance analysis of nmpc: Detectable stage costs and general terminal costs," *IEEE Transactions on Automatic Control,*

68(10), pp. 6114–6129.

[26] Zavala, V. M., and Biegler, L. T., 2009, "The advanced-step nmpc controller: Optimality, stability and robustness," *Automatica,* **45**(1), pp. 86–93.

[27] Camacho, E. F., and Bordons, C., 2016, *Model predictive control: Classical, robust and stochastic* Springer International Publishing.

[28] Liu, Y., Druyor, C. T., and Wang, L., 2023, "High-fidelity analysis of Lift+ Cruise VTOL urban air mobility concept aircraft," In AIAA AVIATION 2023 Forum, p. 3671.

[29] Johnson, W., and Silva, C., 2022, "NASA concept vehicles and the engineering of advanced air mobility aircraft," *The Aeronautical Journal,* **126**(1295), pp. 59–91.

[30] Patterson, M. D., Antcliff, K. R., and Kohlman, L. W., 2018, "A proposed approach to studying urban air mobility missions including an initial exploration of mission requirements," In Annual Forum and Technology Display, no. NF1676L-28586.

APPENDIX A: CONTROLLERS SETTINGS

The tables presented in this Appendix include the summary of the open loop and controller settings for each simulation case presented. The case ID follows the naming convention "1-2-3", where:

- 1: open-loop (O), LQR (L), MPC (M) or NMPC (N) simulations;
- 2: Vibration or trajectory type: VIB for vibration suppression, LAT for lateral path tracking, LON for longitudinal path tracking;
- 3: addition information, when applicable.

Below is a list of all parameters included in the tables and its meaning.

- Description: description of simulation case
- Tiltrotor initial angle: $90°$ for upwards
  t_f: length of simulation in seconds
- dt: simulation time step in seconds
- Input vector: applicable for NMPC. Open-loop uses all system inputs
- p: NMPC prediction horizon
- n: NMPC control horizon
- Output weight ω^y: weights for each y variable before and after control failure
- Output weight ω^u: weights for each u variable before and after control failure
- $\pm u_{lim}$: upper and lower limits for NMPC inputs
- $\pm \Delta u_{lim}$: upper and lower limits for NMPC input rate

Table 7: Setting for Vibration Suppression and Path Tracking Analysis

Case ID	Description	Rotor initial angle, deg	t_f, s	dt, s	Output vector $\mathbf{y}$	Input vector $\mathbf{u}$	p	n	Output weight $\omega^{\mathbf{y}}$	Input weight $\omega^{\mathbf{u}}$	$\pm\mathbf{u}_{\mathbf{lim}}$	$\pm\Delta\mathbf{u}_{\mathbf{lim}}$
O-VIB	Open loop results for vibration suppression.	$\{90, 90, 0, 0, 90, 90\}$	80	0.01	$\{\phi, \theta, \psi, p^G_{B,x}, p^G_{B,z}\}$	Eq. 8	-	-	-	-	-	-
O-VIB-30	Open loop results for vibration suppression with 30% of elevator excitation.	$\{90, 90, 0, 0, 90, 90\}$	80	0.01	$\{\phi, \theta, \psi, p^G_{B,x}, p^G_{B,z}\}$	Eq. 8	-	-	-	-	-	-
L-VIB	LQR results for vibration suppression.	$\{90, 90, 0, 0, 90, 90\}$	80	0.01	$\{\beta, \phi, \theta, \psi, p^G_{B,x}, p^G_{B,z}\}$	$\{\delta_e, \delta_a, \delta_r, \ddot{\Gamma}_{3:4}\}$	-	-	-	-	-	-
L-LAT	LQR results for lateral trajectory path tracking.	$\{90, 90, 0, 0, 90, 90\}$	70	0.01	$\{\beta, \phi, \theta, \psi, p^G_{B,x}, p^G_{B,y}, p^G_{B,z}\}$	$\{\delta_e, \delta_a, \delta_r, \ddot{\Gamma}_{3:4}\}$	-	-	-	-	-	-
L-LON	LQR results for longitudinal trajectory path tracking.	$\{90, 90, 0, 0, 90, 90\}$	180	0.01	$\{\beta, \phi, \theta, \psi, p^G_{B,x}, p^G_{B,y}, p^G_{B,z}\}$	$\{\delta_e, \delta_a, \delta_r, \ddot{\Gamma}_{3:4}\}$	-	-	-	-	-	-
M-VIB	MPC results for vibration suppression.	$\{90, 90, 0, 0, 90, 90\}$	80	0.01	$\{\beta, \phi, \theta, \psi, p^G_{B,x}, p^G_{B,z}\}$	$\{\delta_e, \delta_a, \delta_r, \ddot{\Gamma}_{3:4}\}$	10	-	-	-	$\{25, 25, 25, 100, 100\}$	$\{5, 5, 5, 100, 100\}$
M-VIB-30	MPC results for vibration suppression with 30% of elevator excitation.	$\{90, 90, 0, 0, 90, 90\}$	80	0.01	$\{\beta, \phi, \theta, \psi, p^G_{B,x}, p^G_{B,z}\}$	$\{\delta_e, \delta_a, \delta_r, \ddot{\Gamma}_{3:4}\}$	10	-	-	-	$\{25, 25, 25, 100, 100\}$	$\{5, 5, 5, 100, 100\}$
N-VIB	NMPC results for vibration suppression.	$\{90, 90, 0, 0, 90, 90\}$	80	0.1	$\{\phi, \theta, \psi, p^G_{B,x}, p^G_{B,z}\}$	$\{\delta_e, \delta_a, \delta_r, \ddot{\Gamma}_{3:4}\}$	10	1	$\{0.5, 5, 0.5, 0.5, 2\}$	$\{0.1, 1, 1, 1.5, 1.5\}$	$\{25, 25, 25, Inf, Inf\}$	$\{5, 5, 5, Inf, Inf\}$
N-LAT	NMPC results for lateral trajectory path tracking.	$\{90, 90, 0, 0, 90, 90\}$	70	0.01	$\{\phi, \theta, \psi, p^G_{B,x}, p^G_{B,y}, p^G_{B,z}\}$	$\{\delta_e, \delta_a, \delta_r, \ddot{\Gamma}_{3:4}\}$	5	2	$\{5, 0.5, 1, 1, 1, 0.5\}$	$\{0.2, 0.2, 0.2, 0.2, 0.2\}$	$\{25, 25, 25, Inf, Inf\}$	$\{5, 5, 5, Inf, Inf\}$
N-LON	NMPC results for longitudinal trajectory path tracking.	$\{90, 90, 0, 0, 90, 90\}$	180	0.01	$\{\phi, \theta, \psi, p^G_{B,x}, p^G_{B,z}\}$	$\{\delta_e, \delta_a, \delta_r, \ddot{\Gamma}_{3:4}\}$	5	4	$\{0.5, 5, 0.5, 0.5, 1\}$	$\{2, 0.2, 0.2, 0.2, 0.2\}$	$\{25, 25, 25, 3500, 3500\}$	$\{5, 5, 5, 3500, 3500\}$

LIST OF FIGURES

LIST OF TABLES